Information merging and reconstruction of single-shot dual-mode wide-field imaging with high spatial resolution Ⓕ

Xuanke Zeng Ⓘ ; Kaipeng Wu; Congying Wang; Yi Cai; Dongmei Huang Ⓘ ; Xiaowei Lu Ⓘ ; Ran Ning; Dongping Zhang Ⓘ ; Wenzhao He; Zhu Wang; Shixiang Xu ✉ Ⓘ ; Jingzhen Li Ⓘ

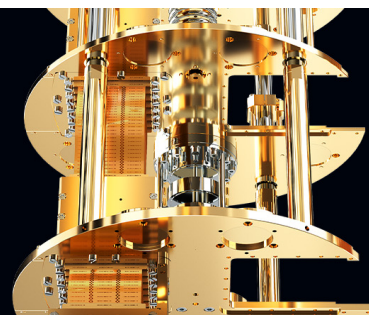# Information merging and reconstruction of single-shot dual-mode wide-field imaging with high spatial resolution ⓕ

Xuanke Zeng,[1] ⓘD Kaipeng Wu,[1] Congying Wang,[1] Yi Cai,[1] Dongmei Huang,[2] ⓘD Xiaowei Lu,[1,a)] ⓘD Ran Ning,[1] Dongping Zhang,[1] ⓘD Wenzhao He,[1] Zhu Wang,[1] Shixiang Xu,[1,b)] ⓘD and Jingzhen Li[1] ⓘD

AFFILIATIONS

[1]State Key Laboratory of Radio Frequency Heterogeneous Integration (Shenzhen University), Key Laboratory of Optoelectronic Devices and Systems of Ministry of Education and Guangdong Province, Shenzhen Key Lab of Micro-Nano Photonic Information Technology, College of Physics and Optoelectronic Engineering, Shenzhen University, Shenzhen 518060, China
[2]Photonics Research Centre Department of Electrical Engineering, The Hong Kong Polytechnic University, Kowloon, Hong Kong, SAR 999077, China

a)Electronic mail: xiaoweilu@szu.edu.cn
b)Author to whom correspondence should be addressed: shxxu@szu.edu.cn

ABSTRACT

In many scenarios, it is really desirable but challenging for wide-field imaging to gather both the clear morphologies and fine details of the target. This paper realizes this imaging by a dual-mode imaging on optical parametric amplification (OPA) with a vortex laser pump. This design includes signal imaging and idler imaging, which have complementary point spread functions with each other. The signal acts as bright-field imaging to record morphologic information, whereas the idler does so for spiral phase contrast imaging to capture the featured details with high brightness and contrast, which has been experimentally confirmed with a target of herb tissue. By utilizing the coupling relation among the pump, signal, and idler, the information from the recorded signal and idler images can be merged, which allows us to reconstruct the target picture owning both high-contrast morphologies and high-brightness fine details. Due to high OPA gain, our imaging can work with weak illumination. Its field-of-view covers an area of 0.33×0.33 mm^2 with a spatial resolution up to 228 lp/mm. This OPA imaging also provides an effective way for the imaging required nonlinear frequency conversion.

In general, it should start with a brief introduction, followed by other sections. Bright-field microscopy,[1–3] as the most basic and commonly used imaging mode, can collect information on the low-frequency part of the samples and is easy to operate. Therefore, it has been widely applied in observing life science phenomena,[4–7] detecting material properties,[8,9] and other fields. This kind of imaging is usually used to obtain entire morphology information of objects and can operate well for samples with intensity modulation. However, in many scenarios, e.g., for some biological cell tissue, the focus may be on the fine structure information of the targets;[10] for some highly transparent samples, phase-imaging is required. Dark-field imaging[11,12] can be used to observe phase objects, but it loses a lot of image intensity because the low-frequency information is entirely filtered out by a high-pass filter. Optical phase contrast imaging (PCI) emerges as one of the most effective ways for the objective detection and

recognition,[13–15] allowing to realize not only the edge enhancement for amplitude patterns but also the conversion of non-visible phase patterns to intensity information. Spiral PCI[16–19] with some spiral phase modulations can work well for phase-filtering due to isotropic edge detection.[20,21] It was experimentally proved that spiral PCI has better brightness and contrast than the traditional dark-field imaging.[16]

Spiral PCI can underscore the fine structure information but often loses a lot of bright-field information of the samples. Accordingly, some efforts have been made to get both bright-field imaging and spiral PCI by incorporating an all-dielectric metasurface in a Fourier transform setup[22] or using a dual-mode metalens integrated with a liquid crystal cell to electrically switch the imaging modes.[23] However, the two imaging methods work by controlling the incident circular polarization states, thereby failing to achieve entire the morphology together with the fine structure information of the

targets simultaneously. In 2023, Zhang *et al.*[24] proposed a design and got simultaneously two spatially separated images: one belongs to spiral PCI and another to bright-field imaging by using a dielectric metasurface with an optical aperture of 1 mm. However, the small apertures of metasurface devices[22–24] may usually limit the field of view to submillimeter level.

Optical parametric amplification (OPA) imaging has drawn considerable attention for decades due to its unique properties.[25] As is known, in traditional OPA imaging with Gaussian beam, the imaging characteristics of the signal is similar to that of the idler. However, if pumped by a vortex laser, detail enhancement can be realized in the idler imaging,[26] which means that, by some appropriate design, complementary point spread functions are available for the signal and idler imaging. Here, we realize OPA imaging on the Fourier plane with a vortex pump but a Gaussian seed, which can work for simultaneous signal and idler dual-mode imaging with complementary point spread functions. Our experiments show the signal can present the entire morphology information, while the idler records enhanced fine structures of the samples with the millimeter level field of view. Interestingly, due to the nonlinear three-wave coupling among the pump, signal, and idler, the information from the recorded signal and idler images can be merged, which allows us to synthetize the information from the bright-field signal and spiral PCI idler images, and reconstruct the target picture owning both high-contrast morphologies and fine details with high brightness. This dual-mode imaging provides an effective way for noninvasive observation of a target from the entire morphology to fine detail views with high gain and contrast in single-shot mode.

The setup of the single-shot dual-mode imaging system is illustrated by Fig. 1, where a nonlinear crystal is set at focal plane of the lens L-1 for OPA. Another two lenses (L-2 and L-3) are arranged confocally with L-1 to form two 4-*f* imaging systems. In this setup, the weak signal illumination goes through a target and has the Fourier spectrum at the focal plane of L-1, which then works as the signal of OPA. A vortex laser pulse as the pump of OPA is achieved by using a spiral phase plate (SPP), which is imaged at the front surface of the OPA crystal. After OPA, the amplified signal and the generated idler propagate non-collinearly under the phase-matching constraint, so that they can be Fourier-transformed by the lenses L-2 and L-3 to get spatially separated images and recorded by two separated CCD cameras at the imaging plane of the two 4-*f* imaging systems.

Suppose that the incident signal light of the object is $E_s(r, \phi, \lambda_s)$, correspondingly, on the Fourier plane, the light field can be described by its Fourier transform $E_{sf}(\rho, \varphi, \lambda_s)$. Unlike traditional spiral PCI,[16–21] here we introduce a nonlinear vortex filter by OPA with vortex pump.
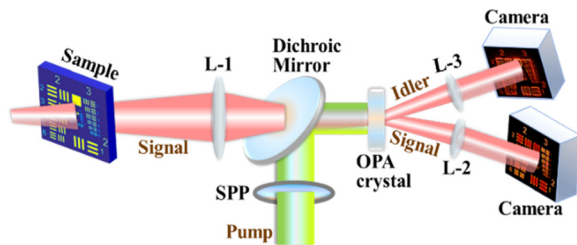
FIG. 1. The setup of the dual-mode OPA imaging system. SPP: Spiral phase plate; L-1–L-3: Lenses.

Under the paraxial approximation and the slowly varying amplitude approximation, the signal and idler light field in the Fourier plane can be described by the coupled wave equations as

$$
\begin{aligned}
\frac{\partial E_{sf}(\rho, \varphi, \omega_s)}{\partial z} &= -i\frac{\omega_s d_{eff}}{n_s c} E'_{if}(\rho, \varphi, \omega_i) A_p e(-i\Delta kz), \\
\frac{\partial E_{if}(\rho, \varphi, \omega_i)}{\partial z} &= -i\frac{\omega_i d_{eff}}{n_i c} E'_{sf}(\rho, \varphi, \omega_s) A_p e^{il\varphi_p} e(-i\Delta kz),
\end{aligned}
\tag{1}
$$

where the superscript "*'*" stands for conjugate, the subscripts "*s*", "*i*," and "*p*" represent signal, idler, and pump, respectively. d_{eff} represents the effective nonlinear coefficient, and n is the refractive index, A is the complex amplitude, while l is the topological charge, thus $l\varphi_p$ is the vortex phase of the pump. ω is the angular frequency, and Δk stands for the phase mismatching. The idler frequency ω_i has the relation with the pump and signal frequencies (ω_p and ω_s) as $\omega_i = \omega_p - \omega_s$. By considering the small-signal approximation, the output light fields of signal $E_{sout}(r, \phi, \omega_s)$ and idler $E_{iout}(r, \phi, \omega_i)$ at the imaging plane shall be

$$
\begin{aligned}
E_{sout}(r, \phi, \omega_s) &= \Im^{-1}\big[E_{sf}(\rho, \varphi, \omega_s)\big] \\
&= G_s E_s(r, \phi, \omega_s) * \Im\big[A_{pn}(\rho, \varphi, \omega_p)\big], \\
E_{iout}(r, \phi, \omega_i) &= \Im^{-1}\big[E_{if}(\rho, \varphi, \omega_s)\big] \\
&= G_i E'_s(r, \phi, \omega_s) * \Im\big[A_{pn} e^{il\varphi_p}(\rho, \varphi, \omega_p)\big],
\end{aligned}
\tag{2}
$$

where "$*$" stands for the convolution and "$\Im$" is the operator of Fourier transformation. G_s and G_i are the OPA gains of signal and idler, A_{pn} is the normalized amplitude of the pump electric field. During the OPA process, the vortex pump phase can be copied to the idler but not to the signal.[25,27] That is to say, the vortex pulse not only serves as an OPA pump but also imposes a vortex phase modulation for the idler but an amplitude filter for the signal.

In Eq. (2), for a traditional OPA imaging pumped by a Gaussian beam with a topological charge of $l = 0$, $E_{sout}(r, \phi, \omega_s)$ and $E_{iout}(r, \phi, \omega_i)$ are approximately equal with similar gains of G_s and G_i. However, if a vortex pump with a non-zero topological charge is used, G_s and G_i are still similar when SPP imaging to the position of OPA crystal, but $E_{iout}(r, \phi, \omega_s)$ with the spiral phase term exp $(il\varphi_p)$ is different from $E_{sout}(r, \phi, \omega_i)$, thereby results in different spatial mode of idler from the signal.

According to Eq. (2), we can get the signal and idler point spread functions $h_s(r, \phi, \omega_s)$ and $h_i(r, \phi, \omega_i)$. Figure 2 are the calculated radial distributions of the signal (black) and idler (red) point spread functions when $l = 1$. Obviously, $h_i(r, \phi, \omega_i)$ has its two main peaks situated symmetrically around the beam center, whereas $h_s(r, \phi, \omega_s)$ locates its sole peak at the center as the nonlinear crystal is set at the imaging plane of the SPP. One can see that the differences of $h_s(r, \phi, \omega_s)$ and $h_i(r, \phi, \omega_i)$ form a natural complementarity to collect target information, allowing to obtain edge-enhanced information in the idler image while the entire morphology information in the signal image with the same OPA. Accordingly, much richer target features can be flexibly extracted by combining the signal and the idler information with different weights. Of course, the spiral phase with high-order l values can also be used for the edge enhancement. As l value increases, our calculations show the twin peaks in the idler point spread function will move symmetrically away from the center. By comparison, $l = 1$ is chosen here for better information complementation between the signal and idler images.
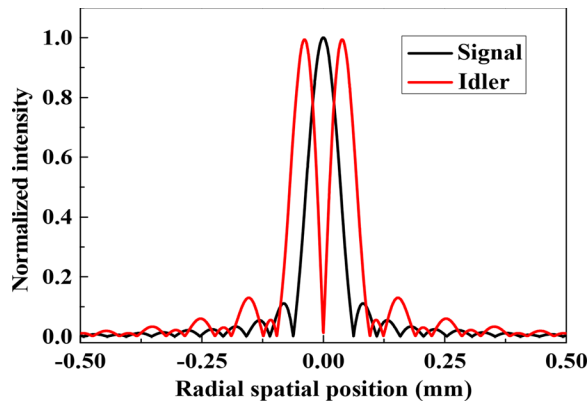
FIG. 2. The radial spatial distribution of point spread functions for signal and idler imaging when $l = 1$.

Figure 3 presents some numerical simulations according to the following experimental conditions described in the subsequent experiment with a USAF 1951 resolution chart as the sample. As predicted, our simulations show the detail-enhanced effect in the idler image but the entire morphology in the signal image at the same time, as shown in Figs. 3(a) and 3(b), respectively, which is easy to be explained by Fig. 2. Due to the coupling relation among the pump, signal, and idler, an image can easily be extracted by merging the signal and idler information, thus containing richer sample information. According to our experimental conditions, the OPA gain has been measured at 6. Accordingly, we merged the signal and idler images with a normalized intensity proportion of 6:5 to reconstruct the image. As shown in Fig. 3(c), both the entire bright-field morphology and the detail-enhanced features of the sample are clearly displayed there, which means this dual-mode OPA imaging can help to get much more visible imaging information.

In order to realize our dual-mode OPA imaging based on Fig. 1, a mode-locked Nd: YAG laser is used as the light source outputting 30 ps-1064 nm light pulse with a maximal pulse energy of 5 mJ. A small part of the output, about 6 μJ/cm^2, is used as the week illumination and the signal for OPA imaging. A 24.3°-cut, 4 mm thick KTP crystal with a clear aperture of 8×8 mm^2 is chosen as the OPA crystal due to the high effective nonlinear coefficient of KTP, which is pumped by the second harmonic of the 1064 laser with a beam diameter of 6 mm

at $1/e^2$ of the maximal intensity. The topological charge l of SPP is set at 1 for detail enhancement of the idler imaging. Three-wave interaction for OPA occurs with an OPA gain of 6, when both the signal and the pump overlap spatially and temporally inside the KTP crystal by a non-collinear angle of 2° between the signal and the pump. As predicted by energy conservation, the 1064 nm idler is generated and propagates non-collinearly with the signal, so the signal and the idler images can be directly recorded by the respective CCD cameras (Basler, Aca-600gm).

To check the ability of our dual-mode OPA imaging by vortex pump, we use a resolution chart of USAF 1951 pattern as a target in the experiments. First, a weak signal is used to illuminate to the target. As shown in Fig. 4(a0), the recorded image directly with CCD camera appears to be insufficient brightness. Figures 4(a1) and 4(a2) show the signal and idler images recorded by CCD1 and CCD2 at 1X magnification, respectively. Compared with the traditional spiral PCI without OPA, the vortex pump combines spiral PCI with OPA, which helps the system to realize spiral PCI imaging with high gain and high contrast. So, Figs. 4(a1) and 4(a2), which have been recorded after OPA with an optical gain of 6, have good brightness and image ratio. Similar to the simulation results in Fig. 3, the signal image in Fig. 4(a1) displays the entire bright-field morphology information while the idler shown in Fig. 4(a2) presents the detail-enhanced structures of the target. In Figs. 4(a1) and 4(a2), we can resolve the spatial features from 1 to 22.6 lp/mm (element 4, group 4 of the resolution chart) in the signal image, and from 1 to 20.16 lp/mm (element 3, group 4) in the idler image with a field of view 3.8×3.8 mm^2. Figures 4(b1) and 4(b2) are the recorded signal and idler images when the 1X lens is replaced by a $20\times$ microscope (Olympus, RMS20X, 0.4NA). The former can clearly distinguish the spatial features of resolution chart from 64 (element 1, group 6) to 228 lp/mm (element 6, group 7), while the latter can show clear features from 64 (element 1, group 6) to 181 lp/mm (element 4, group 7). One can see the signal image has higher spatial resolution, whereas the idler owns better imaging contrast. Figure 4(c) shows the local one-dimensional intensity profile of group 2.3 marked with the white arrows in Figs. 4(a1) and 4(a2). The contrast values have been estimated to be 0.47 and 0.7 for the signal (black) and the idler (red) images, respectively, which were calculated by $(I_{max} - I_{min})/(I_{max} + I_{min})$ with I_{max} for the maximal intensity and I_{min} for the minimal intensity of group 2.3. Obviously, due to the suppression of low-frequency background by the vortex pump, the contrast of the idler image is 1.49 times that of the signal image.
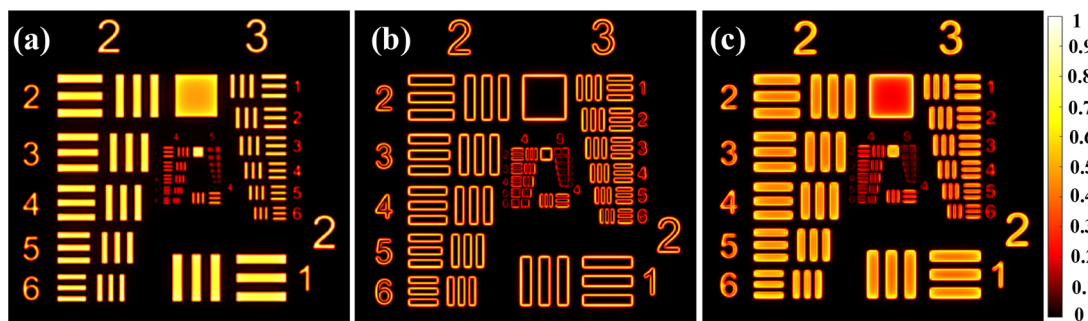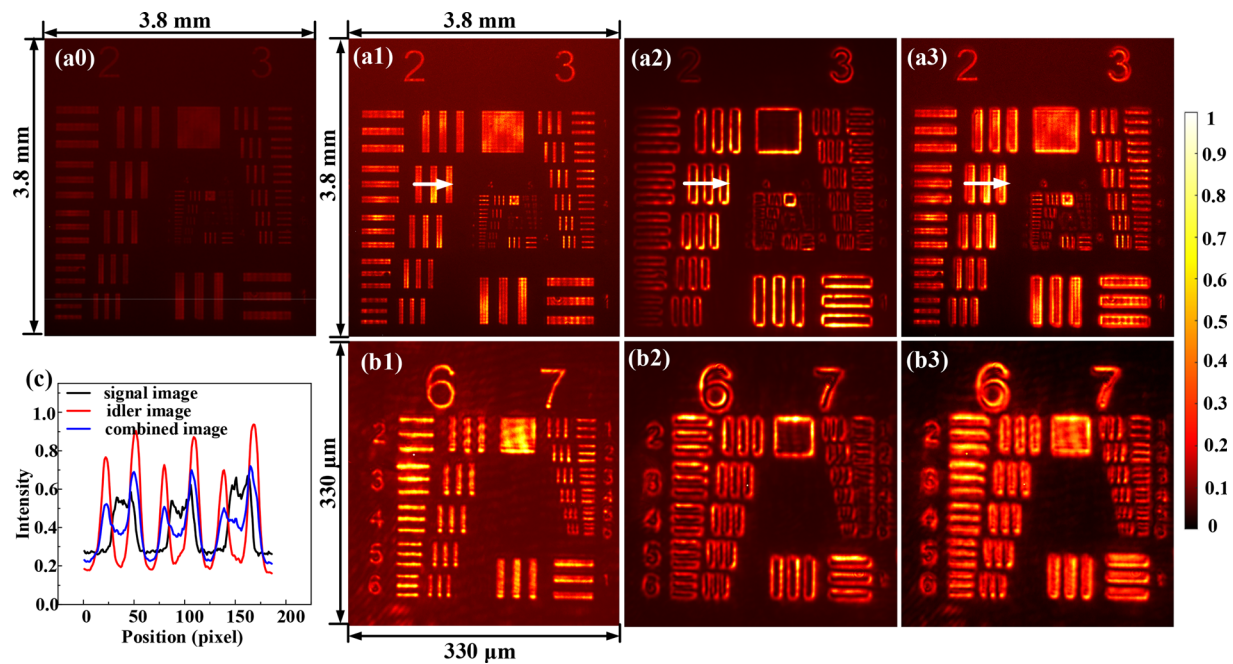

FIG. 3. The simulations of the dual-mode OPA imaging. (a) Signal image, (b) idler image, and (c) a merged image.

FIG. 4. The dual-mode OPA imaging for a USAF 1951 resolution chart pattern. (a0) the signal image illuminated by a weak light before OPA, (a1) the signal, (a2) idler, and (a3) merged images after OPA with 1X optical magnification; (b1) the signal, (b2) idler, and (b3) merged images after OPA by 20X optical magnification; and (c) the local one-dimensional intensity profile of group 2.3 marked with the white arrows in (a1)–(a3).

It is very interesting and meaningful if we can merge the bright-field morphology and fine features into one image. Here, we propose a merging method, which includes two steps. The first step is to calibrate the spatial position correspondence of two CCD cameras used to record the signal and idler images with pixel level accuracy by using the features of a resolution chart pattern as the target. Then, the information of the signal and the idler images are merged via. Eq. (1). Based on Figs. 4(a1)–4(a3) is a merged image by setting an intensity ratio of the signal to the idler to be 6:5 with an OPA gain of 6. It is shown that the merged image has the same spatial resolution as the signal image, but its contrast reaches to 0.59, which is 1.26 times that of the signal image. The image of Fig. 4(b3) has been merged from Figs. 4(b1) and 4(b2). As can be seen, Fig. 4(b3) has got richer sample information: owing both the entire morphology and the clear fine structure information of the samples, meanwhile maintaining high spatial resolution and good imaging contrast.

Now, a thin sample of herb tissue is used as the target to replace the spatial resolution chart. The recorded signal and idler images are shown in Figs. 5(a) and 5(f). Here, a $40\times$ microscope (Olympus, RMS40X, 0.65NA) is used to see the structures with the spatial features finer than 228 lp/mm. One can see that the signal image in Fig. 5(a) shows the bright-field morphology of the biological sample with low-frequency components, but some edge information is blurry or even lost. On the contrary, the idler image in Fig. 5(f) displays clearly the fine details and edges with high contrast, but the low-frequency morphologies with low brightness. For example, in Fig. 5(a), the signal image within the blue box shows clearly that the intensity distribution from the sample increases gradually from the left bottom to the right top, which indicates that the sample has a curved surface. However,

the idler image always has a dark intensity distribution inside the blue zone, so it is hard to see the surface morphology of the sample. Inside the green box of Fig. 5(a), the signal image presents very blurry fine details, which are very clear in Fig. 5(f). These results verified again that the signal imaging can effectively work as bright-field imaging to capture the gradient of the entire morphology information, while the idler imaging does as spiral PCI to suppress the background, meanwhile augmenting the abrupt structure information of the sample. Benefitting from the natural complementary between signal and idler images, we have synthetized the information of Figs. 5(a) and 5(f) to make the reconstructed image be truer, as shown in Figs. 5(b)–5(e). Figure 5(c) is directly obtained based on the three-wave coupling relation among the pump, which means the ratio of the signal to idler is 6:5. As predicted, it shows both morphologies and fine details of the target. Obviously, the signal or idler intensity can be changed with an optical attenuator in front of either CCD1 or CCD2, which allows us to synthetize the signal and idler information with different intensity proportions. Figure 5(b) is obtained by attenuating the idler intensity to have an intensity ratio of 6:2, where the bright field reveals clearly the surface morphology, as well as some not so clear fine structures. With a decrease in the intensity ratio, 3:5 for Fig. 5(d) and 2:5 for Fig. 5(e), the synthetized image strengthens gradually the fine structures, meanwhile weakens the slowly changing surface morphology.

Figure 6 focuses on the local information of the green box in Figs. 5(a) or 5(f) but presents it with two-dimensional spatial intensity in order to better display the imaging features of the sample corresponding to those in Fig. 5. In the bright-field signal image in Fig. 6(a), one can see there is an elliptical area with a hill-like profile that is surrounded by a ditch. Except these, finer details are not so clear. In the
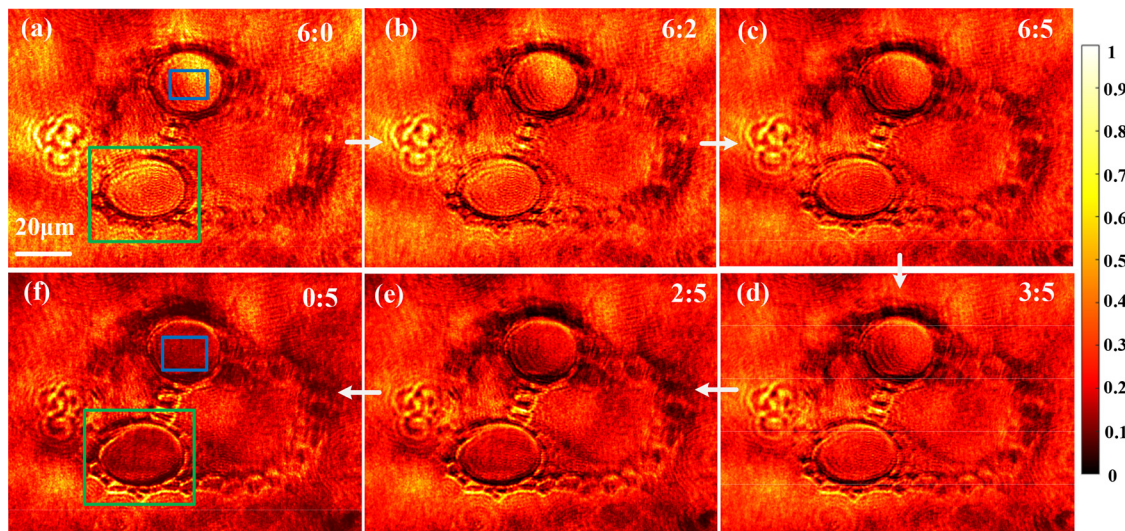
FIG. 5. The dual-mode OPA microscopic imaging for the biological tissue sample. (a) The signal image, (b)–(e) the synthetized images with different intensity ratios, and (f) the idler image.

idler image as shown in Fig. 6(f), many small black specks appear instead of the bright hill-like profile in the elliptical area in Fig. 6(a). Figure 6(f) can also present the elliptical area with a steep border and many tiny peak-shaped features, which fail to be seen in Fig. 6(a), especially in the zone surrounding the point (35, 15). In addition, the high brightness occurs in the zones with the plunging structures or high-frequency details in Fig. 6(f), rather than the slow-extending or low-frequency morphologies in Fig. 6(a). Figures 6(b)–6(e) correspond to Figs. 5(b)–5(e). As the intensity ratio of the signal to the idler decreases, it is clear that the synthetized image moves gradually the

highlights from the low-frequency morphologies to the high-frequency details. These results mean that this dual-mode imaging system can provide the images according to customer preference between the morphologies and fine details by single-shot mode.

In summary, this paper has proposed and realized a dual-mode imaging to gather both the clear morphologies and fine details of the target with high optical gain and enhanced contrast, which is based on vortex pumped OPA. As is known, traditional OPA imaging pumped by a TEM_{00} laser has its signal and idler imaging to own similar performances due to the similar point spread functions, so it usually
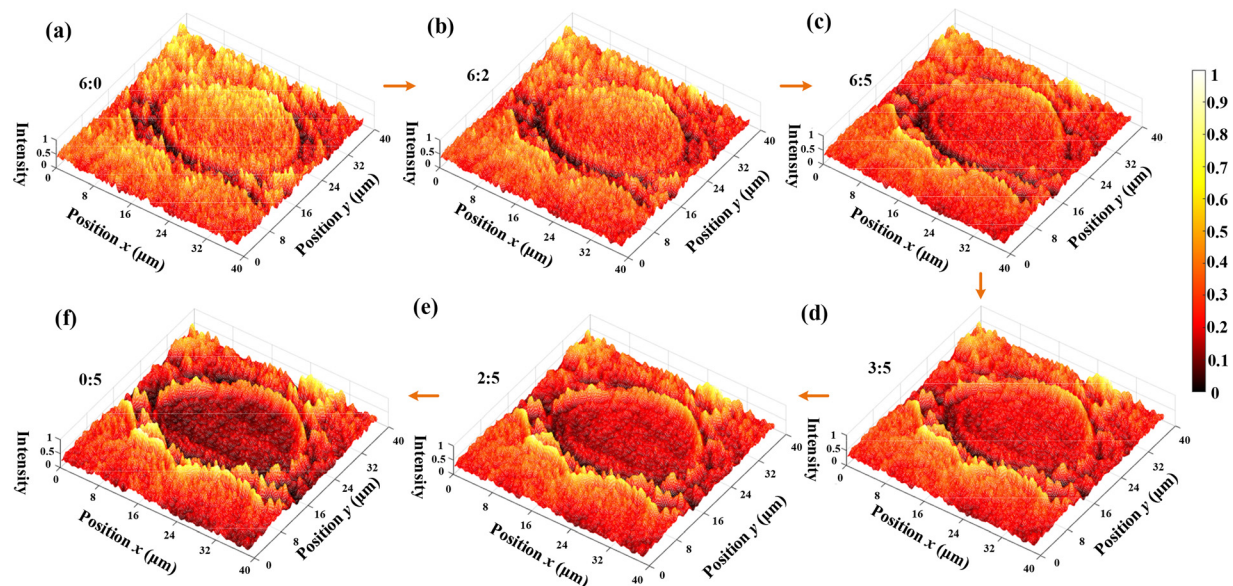
FIG. 6. The local images of the green box in Fig. 5(a) or 5(f) with two-dimensionally spatial intensity corresponding to Figs. 5(a)–5(f).

works for optical imaging with high gain, high sensitivity, and nonlinear frequency conversion. However, if pumped by a vortex laser, the similarity can be replaced by the complementation of the point spread functions. The signal acts as bright-field imaging to record morphologic information, whereas the idler does so for spiral phase contrast imaging to capture the featured details with high contrast, which has been experimentally calibrated with a resolution chart of the USAF 1951 pattern. Furthermore, by using an herb tissue sample, our experiments have captured simultaneously the entire morphology in the signal image and enhanced details with high brightness in the idler image. By utilizing the three-wave coupling among the pump, signal, and idler, the information from the recorded signal and idler images can be merged so that the information from the bright-field signal and spiral phase contrast idler images can be synthetized to reconstruct the target picture owning both clear morphologies and high-brightness fine details. If changing the signal or idler intensity with an attenuator, it allows us to synthetize the signal and idler information with different intensity proportions according to customer preference between the morphology and fine details by single-shot detection. Due to high OPA gain, our imaging can work with weak illumination. Its field-of-view depends on the pump intensity, which allows our imaging to cover an area of $3.8 \times 3.8 \, \text{mm}^2$. This work provides an effective way for noninvasive imaging from entire morphology to fine detail views with high gain and contrast in single-shot mode, which can work for optical imaging with nonlinear frequency conversion, too. We believe that this single-shot dual-mode imaging can be applied effectively in many scenarios, e.g., biological tissue imaging.

AUTHOR DECLARATIONS
Conflict of Interest

The authors have no conflicts to disclose.

Author Contributions

Xuangke Zeng and Kaipeng Wu contributed equally to this work.

Xuanke Zeng: Conceptualization (equal); Funding acquisition (equal); Writing – original draft (equal); Writing – review & editing (equal). **Kaipeng Wu:** Data curation (equal); Formal analysis (equal); Writing – original draft (equal). **Congying Wang:** Investigation (equal); Methodology (lead). **Yi Cai:** Conceptualization (supporting); Funding acquisition (equal). **Dongmei Huang:** Conceptualization (supporting); Validation (equal); Visualization (equal). **Xiaowei Lu:** Conceptualization (supporting); Funding acquisition (equal); Investigation (supporting); Supervision (equal). **Ran Ning:** Formal analysis (lead). **Dongping Zhang:** Conceptualization (supporting). **Wenzhao He:** Investigation (equal). **Zhu Wang:** Data curation (equal). **Shixiang Xu:** Conceptualization (lead); Funding acquisition (lead); Supervision (lead); Writing – review & editing (equal). **Jingzhen Li:** Conceptualization (supporting).

DATA AVAILABILITY

The data that support the findings of this study are available from the corresponding author upon reasonable request.

REFERENCES

[1] Y. Wu, Y. Luo, G. Chaudhari *et al.*, "Bright-field holography: cross-modality deep learning enables snapshot 3D imaging with bright-field contrast using a single hologram," Light **8**, 25 (2019).

[2] S. Helgadottir, B. Midtvedt, J. Pineda *et al.*, "Extracting quantitative biological information from bright-field cell images using deep learning," Biophys. Rev. **2**, 031401 (2021).

[3] Y. J. Yoo, B. Midtvedt, J. Pineda *et al.*, "Gires–Tournois immunoassay platform for label-free bright-field imaging and facile quantification of bioparticles," Adv. Mater. **34**, 2110003 (2022).

[4] L. V. Wang and J. Yao, "A practical guide to photoacoustic tomography in the life sciences," Nat. Methods **13**, 627–638 (2016).

[5] Y. Rivenson, Z. Göröcs, H. Günaydin, Y. Zhang, H. Wang, and A. Ozcan, "Deep learning microscopy," Optica **4**(11), 1437–1443 (2017).

[6] S. D. Findlay, N. Shibata, H. Sawada *et al.*, "Dynamics of annular bright field imaging in scanning transmission electron microscopy," Ultramicroscopy **110**(7), 903–923 (2010).

[7] F. Hu, L. Shi, and W. Min, "Biological imaging of chemical bonds by stimulated Raman scattering microscopy," Nat. Methods **16**, 830–842 (2019).

[8] W. Eschen, L. Loetgering, V. Schuster *et al.*, "Material-specific high-resolution table-top extreme ultraviolet microscopy," Light **11**, 117 (2022).

[9] S. Pujals, N. Feiner-Gracia, P. Delcanale, I. Voets, and L. Albertazzi, "Super-resolution microscopy as a powerful tool to study complex synthetic materials," Nat. Rev. Chem. **3**, 68–84 (2019).

[10] W. Wang, C. Li, Z. Zhan, Z. Zhang, Y. Han, C. Kuang, and X. Liu, "Dual-modulation difference stimulated emission depletion microscopy to suppress the background signal," Adv. Photonics **4**(4), 046001 (2022).

[11] I. Sack, "Magnetic resonance elastography from fundamental soft-tissue mechanics to diagnostic imaging," Nat. Rev. Phys. **5**, 25–42 (2022).

[12] Z. Liu, L. Tian, and L. Waller, "Real-time brightfield, darkfield, and phase contrast imaging in a light-emitting diode array microscope," J. Biomed. Opt. **19**(10), 106002 (2014).

[13] F. Zernike, "Phase contrast, a new method for the microscopic observation of transparent objects," Physica **9**(7), 686–698 (1942).

[14] Y. Park, C. Depeursinge, and G. Popescu, "Quantitative phase imaging in biomedicine," Nat. Photonics **12**, 578–589 (2018).

[15] Y. Gao and L. Cao, "Iterative projection meets sparsity regularization: Towards practical single-shot quantitative phase imaging with in-line holography," Light **4**, 37–53 (2023).

[16] S. Furhapter, A. Jesacher, S. Bernet, and M. Ritsch-Marte, "Spiral phase contrast imaging in microscopy," Opt. Express **13**(3), 689–694 (2005).

[17] J. A. Davis, D. E. McNamara, D. M. Cottrell, and J. Campos, "Image processing with the radial Hilbert transform: Theory and experiments," Opt. Lett. **25**(2), 99–101 (2000).

[18] S. B. Wei, S. W. Zhu, and X. C. Yuan, "Image edge enhancement in optical microscopy with a Bessel-like amplitude modulated spiral phase filter," J. Opt. **13**(10), 105704 (2011).

[19] A. Jesacher, S. Furhapter, S. Bernet, and M. Ritsch-Marte, "Shadow effects in spiral phase contrast microscopy," Phys. Rev. Lett. **94**(23), 233902 (2005).

[20] S. B. Wei, S. W. Zhu, and X. C. Yuan, "Image edge-enhancement in optical microscopy with a phase mismatch spiral phase plate," Chin. Opt. Lett. **9**(3), 031001 (2011).

[21] J. K. Wang, W. H. Zhang, Q. Q. Qi, S. S. Zheng, and L. X. Chen, "Gradual edge enhancement in spiral phase contrast imaging with fractional vortex filter," Sci. Rep. **5**, 15826 (2015).

[22]P. Huo, C. Zhang, W. Zhu *et al.*, "Photonic spin-multiplexing metasurface for switchable spiral phase contrast imaging," Nano Lett. **20**, 2791–2798 (2020).

[23]T. Badloe, Y. Kim, J. Kim *et al.*, "Bright-field and edge-enhanced imaging using an electrically tunable dual-mode metalens," ACS Nano **17**, 14678–14685 (2023).

[24]Y. Zhang, P. Lin, P. Huo *et al.*, "Dielectric metasurface for synchronously spiral phase contrast and bright-field imaging," Nano Lett. **23**, 2991–2997 (2023).

[25]P. M. Vaughan and R. Trebino, "Optical-parametric-amplification imaging of complex objects," Opt. Express **19**(9), 8920–8929 (2011).

[26]X. Zeng, C. Wang, H. Wang *et al.*, "Tunable mid-infrared detail-enhanced imaging with micron-level spatial resolution and photon-number resolving sensitivity," Laser Photonics Rev. **17**, 2200446 (2023).

[27]A. Baltuska, T. Fuji, and T. Kobayashi, "Controlling the carrier-envelope phase of ultrashort light pulses with optical parametric amplifiers," Phys. Rev. Lett. **88**(13), 133901 (2002).

15 May 2025 05:39:34